Journal of Constructional Steel Research 215 (2024) 108513

Contents lists available at ScienceDirect

Journal of Constructional Steel Research

journal homepage: www.elsevier.com/locate/jcsr

Fatigue analysis of hybrid steel construction parts using LPBF on hot-rolled steel

Alessandro Menghini [a,*], Martina Chierici [a], Alper Kanyilmaz [a], Ali Gökhan Demir [b], Carlo Andrea Castiglioni [a,d], Filippo Berto [c], Barbara Previtali [b]

[a] Politecnico di Milano, Department of Architecture, Built Environment and Construction Engineering, Piazza Leonardo da Vinci 32, Milan, 20133, Italy
[b] Politecnico di Milano, Department of Mechanical Engineering, Via La Masa 1, Milan, 20156, Italy
[c] Università di Roma Sapienza, Department of Chemical Engineering Materials Environment, Via Eudossiana 18, Rome, 00184, Italy
[d] Fincon Consulting Italia Srl, Via Volturno, 46, Milan, 20124, Italy

ARTICLE INFO

Keywords:
Metal 3D-printing
High cycle fatigue
Hybrid metal AM joints
Build direction

ABSTRACT

Metal additive manufacturing presents significant opportunities in the construction industry by enabling the creation of innovative components and seamless integration with conventional steel parts to form hybrid structures. However, ensuring the long-term performance of such structures, particularly under cyclic loading, requires a comprehensive investigation into the behavior of individual materials and their interfaces. Unfortunately, current European fatigue design standards do not adequately address the unique considerations of metal additive manufacturing. This paper provides a thorough analysis of high-cycle fatigue in butt-joint connections of arc-welded hybrid additive manufactured joints. The study specifically concentrates on the use of arc welding to join an AISI316L plate produced through the Laser Powder Bed Fusion (LPBF) technique with a quarto plate. Experimental tests incorporate engineering stress control and utilize three distinct stress steps to establish S–N curves. The findings highlight the substantial influence of internal defects and their geometric characteristics on stress concentrations and fatigue life. These insights provide valuable understanding regarding the fatigue performance of hybrid additive manufactured joints compared to conventional steel, opening avenues for further research on the integration of metal additive manufacturing components with traditional steel structures.

1. Introduction

The rising demand for efficient utilization of resources in steel structures has spearheaded the investigation of metal additive manufacturing (AM) as a viable solution for crafting structural nodes in the construction sector [1–4]. The endurance of metal AM products under repetitive loading, commonly referred to as fatigue life, has taken center stage in additive manufacturing research [5–7]. The unique microstructural characteristics of metal AM metals, combined with the occurrence of internal defects, significantly influence the initiation and progression of cracks [8,9]. Moreover, in the design of intricate structural steel nodes, fatigue is a key determinant of the product's geometry and assembly sequence [10,11].

When considering welded joints, specific attributes such as the weld opening angle and the weld seam finishing require meticulous examination to ensure that cyclic load-induced stress and strain states do not precipitate brittle failure [12,13]. The investigation of fatigue phenomena in conventional structural nodes is guided by EN1993-1-9 [14], a standard established based on extensive experience and voluminous experimental tests. These tests have facilitated the classification of nodes' details and estimation of their fatigue life.

Previous studies have examined the fatigue life of base metals in metal additive manufacturing [15–19], as well as the behavior of hybrid metal AM steel when joined with other components [20–24]. However, to the best of authors' knowledge, there is a limited number of studies specifically addressing the cyclic loading behavior of hybrid AM joints.

Some studies have specifically explored laser welding of steel plates manufactured through Laser Powder Bed Fusion (LPBF), resulting in modifications to the involved metals [20,21]. For instance, Zhang et al. [20] conducted experiments on grade 316L stainless steel tensile coupon half parts manufactured using powder bed fusion (PBF) and laser welding. The PBF base material exhibited higher strengths and a finer microstructure compared to conventionally produced stainless steel. The horizontal PBF base material demonstrated higher proof

* Corresponding author.
E-mail address: alessandro.menghini@polimi.it (A. Menghini).

https://doi.org/10.1016/j.jcsr.2024.108513
Received 28 November 2023; Received in revised form 18 January 2024; Accepted 29 January 2024
Available online 7 February 2024

stress due to grain growth orientation, while laser weld regions showed lower hardness and strength due to a coarser microstructure. The study concluded that laser welding enables the use of additive manufacturing for large-scale components, but the potentially lower mechanical properties of welds should be taken into account during the design process.

Chierici et al. [24] investigated the mechanical behavior of hybrid steel components formed by welding LPBF plates and quarto plates made of AISI 316L stainless steel. The mechanical characterization of LPBF-produced plates, quarto plates, and the welded hybrid components revealed a maximum difference of 10% in their properties.

The possibility of directly manufacturing components onto existing parts using LPBF technique has also been explored [22,25]. In a study by Merklein et al. [22], a gear component with discrete tooth geometry was manufactured using a combination of powder bed fusion of metal using a laser beam (PBF-LB/M) and a forming process. The study presented a process chain for manufacturing hybrid parts and evaluated the final part geometry through topography measurement.

However, it is important to note that manufacturing parts onto existing parts requires flat surfaces for building the LPBF-produced part and is limited by the volume capacity of the machine used. There is currently a lack of literature on arc welding of LPBF-produced steels, especially in the context of hybrid joints. Pasang et al. [23] demonstrated promising mechanical properties with arc-welded 2.5-mm-thick steel plates produced through LPBF.

Given the relatively small size of metal AM components, a consequence of restricted production chamber dimensions, these parts often need to be assembled with other conventional components to form a complete steel joints, as shown in Fig. 1. Understanding how AM components interact with metals produced through different manufacturing processes, particularly regarding potential modifications in the base material due to employed joining techniques (such as welding), is therefore crucial [26,27]. The potential applications of this technology may be related to the local repair of large structure components [28,29] or the realization of hybrid constructions [30].

In this study, arc welding has been used to create the studied hybrid elements. Indeed, arc welding is a common technique for on-site steel structure assembly that is highly compatible with stainless steel, to join AM nodes. An experimental investigation into the fatigue life of butt-joint produced by arc welding an LPBF AISI316L plate with a quarto plate has been carried out. This joint category is well-documented and regulated by the EN1993-1-9 [14] when made by conventional steel, and this has served as a reference for the experimental study on the hybrid metal AM joints to identify the differences in their behavior.

This paper introduces a methodology for accurately modeling the interaction between hybrid materials and assessing their fatigue resistance in the elastic regime, specifically in the context of incorporating hybrid details in building structures. Subsequently, the study focuses on investigating the high cycle fatigue of arc-welded samples made from hot-rolled and LPBF-produced plates. The S–N curve for the tested samples is determined through tests conducted under engineering stress control, following ASTM E739-10 guidelines [31]. Furthermore, fracture surfaces are examined using a scanning electron microscope to identify crack origins and propagation. Additionally, the results are analyzed using the strain energy density (SED) approach to further explore the correlation between fatigue life and joint build directions.

The study demonstrated that the fatigue life of metal AM parts is significantly influenced by the shape and orientation of the pores, which are determined by the build direction. The insights gained regarding the long-term performance of additive manufacturing (AM) have direct relevance to its application in the construction industry. Fig. 1-a demonstrates the capability of hybrid AM to produce complex three-dimensional shapes with personalized designs and remarkable accuracy. These components can be invaluable for localized repair work in medium–large scale structures (such as complex geometries in Fig. 1-b), allowing for efficient on-site welding without the need for complete structure replacement.

2. Static tensile behavior of hybrid specimens

In the study conducted by Chierici [24], which pertains to the same production plate from which the samples in this study are derived, material properties were analyzed using a 10 mm thick plate, as depicted in Fig. 2. The selection of the test material was based on meeting the standard mechanical properties typically required for metals used in structural applications [32], as well as ensuring its suitability for the LPBF process [33]. The chemical composition of the quarto plate steel can be found in Table 1. The production process, illustrated in Fig. 2, involved the creation of LPBF 10 mm thick plates with various build orientations. To provide a comprehensive characterization of the material, the study by Chierici et al. [24] encompassed evaluations of porosity, microhardness, microstructures, tensile strength, and anisotropy.

The experimental analysis aimed to evaluate the integrity of the welded joint and investigate the impact of welding thermal cycles on the material properties. For the hybrid specimens, six tensile testing bars were obtained by cutting the welded plates. Each testing bar had a length of 143 mm, a thickness of 10 mm, and a width of 10 mm, as depicted in Fig. 3. Tensile tests were conducted using a universal testing machine (MTS Alliance RT/100, Eden Prairie, MN, USA) equipped with a digital image correlation (DIC) system (Aramis 3D Camera, Braunschweig, Germany) to analyze the deformation behavior. Prior to testing, a speckle pattern was applied to the specimens. The DIC system enables precise strain calculations on a predefined region of the sample, providing accurate data on the LPBF and quarto plate sides of the hybrid specimens.

The results, presented in Fig. 4, revealed heterogeneous strain behavior among the welded specimens. Notably, the elongation at ultimate tensile strength ϵ_u of the LPBF part increased by approximately 10% after welding. Additionally, the elongation at failure ϵ_f exhibited higher values compared to the base metals, indicating increased ductility due to the welding thermal cycles. These findings demonstrate the successful weldability of thick LPBF AISI 316L plates and quarto plate parts using arc welding.

The microstructure examination of the welded samples exhibited the expected grain distribution characteristic of the AISI 316L quarto plate. The welding thermal cycles did not affect the grain dimensions, which remained at an average of 30 μm. The weld seam observation revealed a medium width of 3 mm, 30 times larger than the average dimension of the LPBF melt pools. The samples examined in this experimental campaign exhibited a minimal level of anisotropy, indicative of favorable production process parameters and high material quality. The employed process facilitated a uniform distribution of both physical and mechanical properties. Nevertheless, it is crucial to note that even a slight degree of anisotropy in static behavior, often overlooked in static modeling or design, can have implications for fatigue life. In fact, static behavior is primarily influenced by microstructure dimensions and grain orientation, while fatigue life is contingent upon factors such as surface and internal defects, their dimensions, diffusion, and orientation. These findings prompted the authors to delve deeper into the anisotropic nature of this material, especially in terms of fatigue life, to ensure a comprehensive understanding of the significant aspects associated with steel produced through LPBF.

3. Numerical modeling of the hybrid material

Due to the absence of tailored design regulations for 3D-printed structural components, numerical analyses are essential to assess their structural integrity. Material and welded joint modeling follows the methodology proposed by EN1993-1-4 [34] and EN1993-1-5 [35], ensuring the applicability of current design rules to LPBF products. This study investigates two material models: isotropic and transversal isotropic. Both models assume linear elastic behavior up to the 0.1% proof stress to capture the unique material characteristics. The isotropic model, with three axes of symmetry, requires two independent elastic

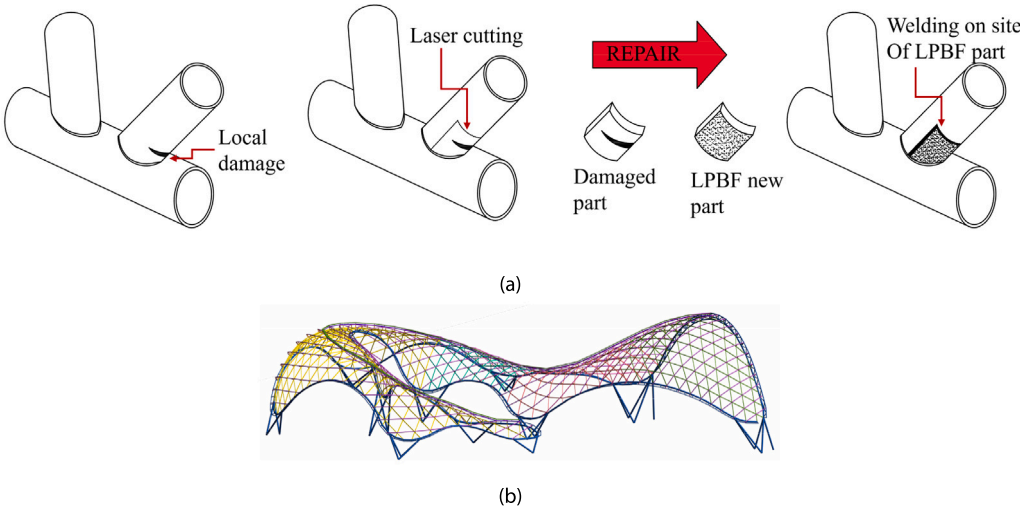

Fig. 1. Hybrid AM connections: (a) Repairing existing structures; (b) Tubular steel canopy.

Table 1
Chemical composition of the quarto plate steel for LPBF.

Mass %	C	Si	Mn	P	S	Cr	Ni	Mo	N	Iron
Quarto Plate	0.017	0.50	1.35	0.027	0.002	17.0	10.1	2.04	0.04	balance

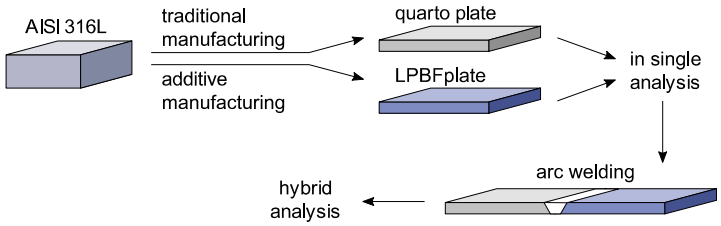

Fig. 2. Processes involved in the production of the sample [24].

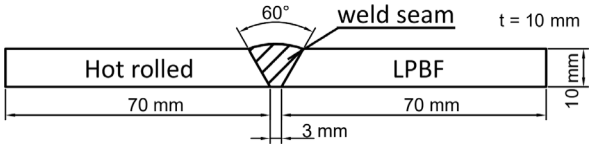

Fig. 3. Hybrid sample geometry (nominal values).

constants (Young's modulus (E) and Poisson's ratio (ν) for modeling). The shear modulus (G), a remaining elastic constant needed for the compliance matrix, is determined by E, ν, and expressed by Eq. (1).

$$G = E\,(1+\nu) \tag{1}$$

The elastic phase of a transversely isotropic material was simulated using the transversely isotropic elastic model, which demonstrates orthotropy with rotational symmetry around axis 3 (Fig. 5). This selection was motivated by the inherent symmetry arising from the layer superimposition that occurs during the printing process. The constitutive equation for this model is defined by five independent elastic constants [36].

Notably, the isotropy observed in the transversal plane (plane 1-2, as illustrated in Fig. 5) permits the utilization of Eq. (2) to derive the shear modulus. Hence, the five independent elastic constants, namely E_1, E_3, ν_{12}, ν_{13}, and G_{13}, respectively represent the elastic modulus in the transversal (isotropic) plane 1-2, the elastic modulus in the plane 1-3, which is perpendicular to the transversal plane, the Poisson's ratio in the transversal plane 1-2, in the normal plane 1-3, and the shear modulus. Consequently, the significant symmetries of the elastic tensor necessitate the compliance matrix to exhibit symmetry, as expressed by Eq. (2). The constitutive equations, when expressed in their inverse form as shown in Eq. (3), emphasize the simplifications resulting from the transition from orthotropy to transverse isotropy:

$$G_{12} = \frac{E_1}{\left[2\left(1+\nu_{12}\right)\right]} \tag{2}$$

$$\begin{bmatrix}\epsilon_{11}\\ \epsilon_{22}\\ \epsilon_{33}\\ \epsilon_{12}\\ \epsilon_{13}\\ \epsilon_{23}\end{bmatrix} = \begin{bmatrix} 1/E_1 & \nu_{12}/E_1 & \nu_{31}/E_1 & 0 & 0 & 0\\ -\nu_{12}/E_3 & 1/E_2 & \nu_{31}/E_1 & 0 & 0 & 0\\ -\nu_{13}/E_3 & \nu_{13}/E_3 & 1/E_3 & 0 & 0 & 0\\ 0 & 0 & 0 & \frac{2(1+\nu_{12})}{E_1} & 0 & 0\\ 0 & 0 & 0 & 0 & 1/G_{13} & 0\\ 0 & 0 & 0 & 0 & 0 & 1/G_{13}\end{bmatrix} \cdot \begin{bmatrix}\sigma_{11}\\ \sigma_{22}\\ \sigma_{33}\\ \sigma_{12}\\ \sigma_{13}\\ \sigma_{23}\end{bmatrix} \tag{3}$$

To construct the material model based on experimental test results, the values of experimental Poisson's ratios, $\bar{\nu}_{13}$ and $\bar{\nu}_{31}$, need adjustment for compliance matrix symmetry. The least-square method has been used, minimizing the sum of the squares (Eq. (4)) of the relative error between experimental and approximated values in Eq. (5). To analyze the impact of anisotropy on this elastic constant, three alternatives are proposed. In these equations, $\bar{\nu}_{ij}$ represents experimental Poisson's ratio, and ν_{ij} denotes the approximated value. Compliance matrix symmetry is enforced by Eqs. (4)–(5).

$$S = \sum_i f^2(x_i) \tag{4}$$

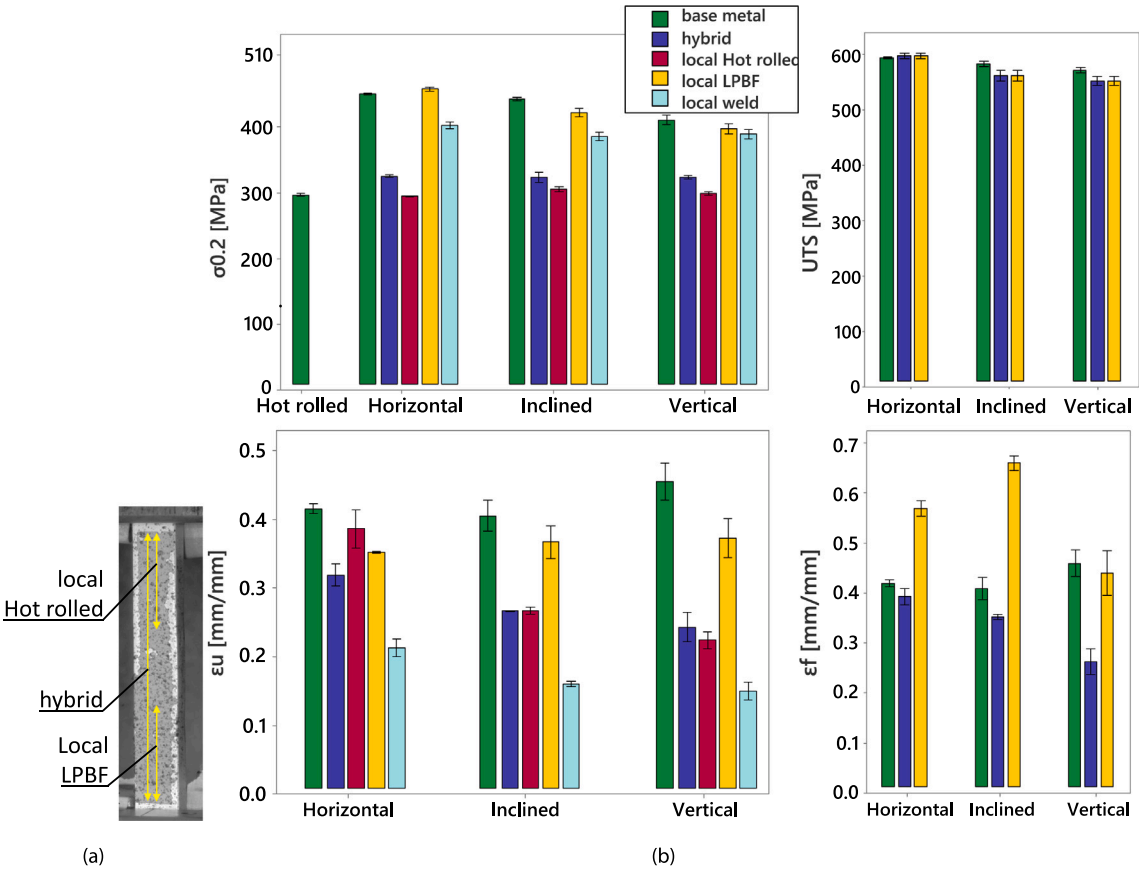

Fig. 4. Mechanical properties of the hybrid samples: (a) strain virtual sensors; (b) local values from the three regions of the welded samples.

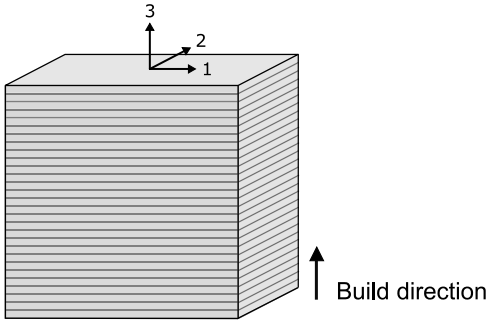

Fig. 5. Scheme of the layered printed part and reference system: build direction (axis 3), scan plane (plane 1-2).

$$f(\nu_{ij}) = \begin{cases} |\bar{\nu}_{ij} - \nu_{ij}| \\ \frac{\bar{\nu}_{ij} - \nu_{ij}}{\nu_{ij}} \\ \frac{\bar{\nu}_{ij} - \nu_{ij}}{E_i} \end{cases} \tag{5}$$

where $i, j = 1, 3$ for $i \neq j$. The transformation equation for the compliance matrix is given by:

$$\nu_{13} E_3 = \nu_{31} E_1 \tag{6}$$

The shear modulus G_{13} for a transversally isotropic material can be expressed as [37], where E_{Incl} is the principal elastic modulus from tensile tests in a 45° off-axis configuration:

$$G_{13} = \frac{1}{\frac{1}{1-\nu_{13}} E_1 + \frac{4}{E_{\text{Incl}}} + \frac{1}{1-\nu_{31}} E_3} \tag{7}$$

3.1. Modeling of elastic deformation using finite element method

Steel AISI316L for structural use is always modeled as isotropic (e.g., EN1993-1-4 [34]). This hypothesis is based on the low degree of anisotropy that steel usually has, but also on the employment of laminated components in steel structures. The rolling direction is always parallel to the components' axis, and the huge experience in components' behavior allowed to define average values of the mechanical properties to guarantee a safe design with an isotropic material behavior. The model adopted in this work considered a linear-elastic curve for the elastic phase of AISI 316L (E=192 MPa, ν=0.3, G=73.8 GPa).

The LPBF steel has not been represented by a complete anisotropic material, but by a transversal isotropic, since the layer-based production generates a plane of isotropy which is orthogonal to the build direction.

Table 2 presents the input values for the LPBF AISI 316L (Inclined build direction) for the finite element formulation. In this paper, the numerical modeling was conducted using the Abaqus software [38].

The elastic parameters were derived from the experimental curves illustrated in Fig. 6 and incorporated into the matrix of the finite element (FE) model, as presented in Eq. (3). The results, specifically the numerical Young's modulus E and Poisson's coefficient ν, exhibit a noteworthy alignment with the experimental values, as demonstrated in Fig. 7. Tests on welded hot-rolled AISI 316L plates bonded via LPBF showed the base metal's mechanical properties largely remained intact post-welding, save for a 10% reduction in break elongation.

After adjusting the model for this reduction, the material models were integrated into the sample geometry (Fig. 2-b). The weld seam's actual geometry was approximated as trapezoidal and assumed to behave like the hot-rolled material. No significant weld bead weaknesses were found; hence, a rigid link was used for connecting the base metals

Table 2
LPBF parameters modeling.

E_1 [GPa]	E_2 [GPa]	E_3 [GPa]	ν_{13} [–]	ν_{31} [–]	ν_{32} [–]	ν_{23} [–]	ν_{12} [–]	ν_{21} [–]	G_{12} [GPa]	G_{13} [GPa]	G_{23} [GPa]
195	195	187	0.33	0.31	0.31	0.33	0.29	0.29	75.40	74.70	74.70

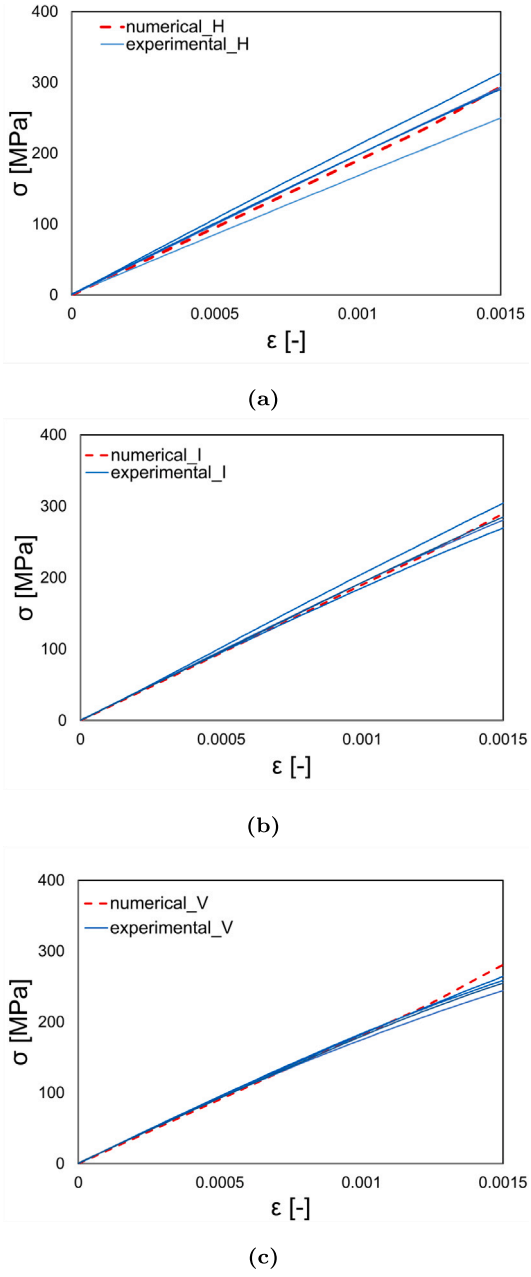

Fig. 6. Elastic behavior of the hybrid specimens (experimental vs numerical):(a) Horizontal direction (H); (b) Diagonal direction (I); (c) Vertical direction (V).

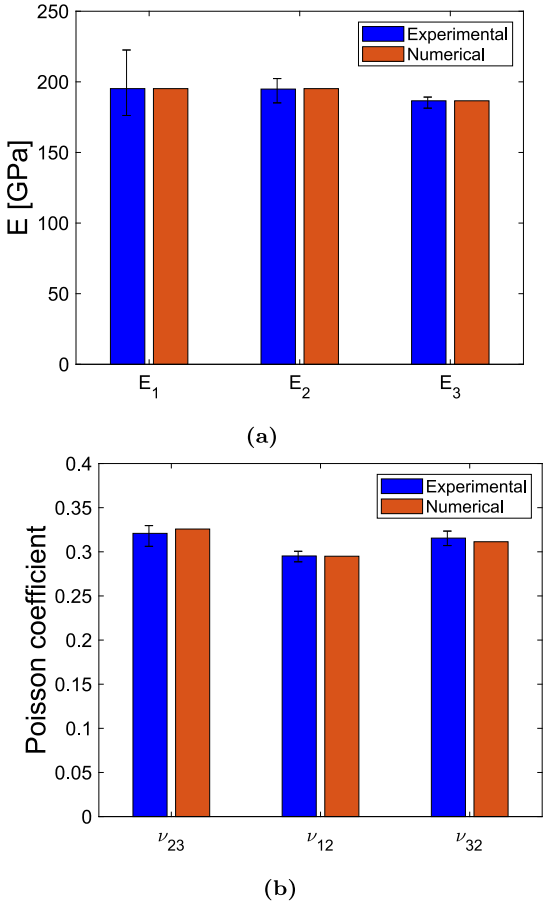

Fig. 7. Calibration of numerical models: (a) Elastic modulus; (b) Poisson's coefficient.

and the weld bead. Model calibration involved a quasi-static load with imposed displacement in the simulation, and results were compared with experimental findings processed through digital image correlation (DIC). The numerical model mirrored the hybrid behavior observed in DIC tensile tests. Strains initially formed in the conventional steel (Fig. 8), then concentrated in the LPBF region, causing necking (Fig. 8).

Given that LPBF is used for producing complex-shaped structural nodes to be assembled with conventional steel parts, the level of anisotropy becomes significant in the overall system's behavior. The orientation of LPBF parts influences the behavior of both the node and the assembled joint with conventional profiles [39,40]. To assess the potential impacts of high anisotropy, the previously described numerical models were utilized for a parametric analysis involving variations in the anisotropy of the LPBF steel (as depicted in Fig. 9). Specifically, the LPBF model maintained consistent properties as presented in Table 2. From a computational standpoint, the material parameters remained constant, while the reference material orientation was adjusted from 0 to 90° (equivalent to 0 to 1.57 rad), as visually depicted in Fig. 9.

4. Testing layout

The fatigue behavior was evaluated and recorded in the form of S–N curves, derived from the test samples. Furthermore, the fracture surface was examined to determine the site of crack formation and to trace the crack propagation path. The entire testing process was regulated under engineering stress control with frequencies ranging from 20 to 35 Hz. Fig. 10 depicts the testing machine alongside the plate from which the samples were extracted. Prior to the commencement of the tests, the cross-sections of the base metals were measured. As depicted in the Fig. 10-b, the weld transition section was intentionally left unsmoothed to assess how it responds to irregular surface finishing, a scenario

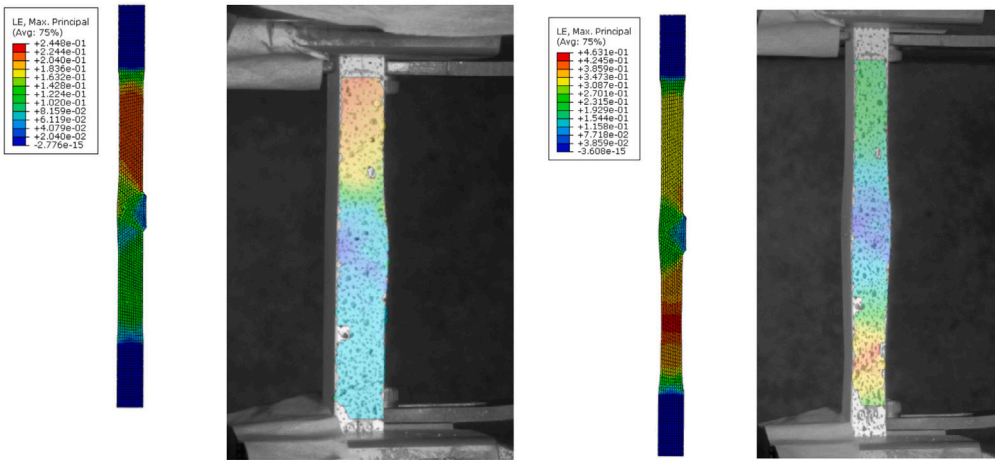

Fig. 8. Strain distribution in the hot rolled-LPBF welded sample from the experimental tests with DIC and the numerical simulations: (a) total strain 0.2; (b) total strain 0.47.

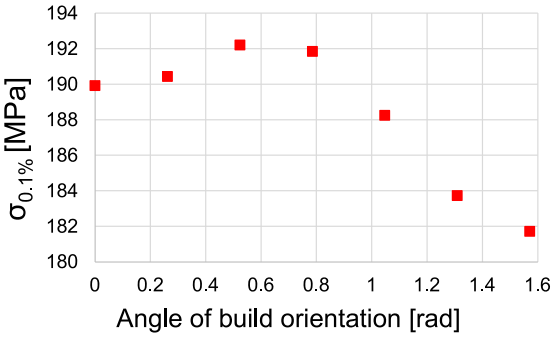

Fig. 9. Material orientation's parametric analysis: 0.1% stress.

that may arise during on-site welding in existing joints. The primary objective was to investigate the factors that predominantly influenced the fatigue strength of samples, specifically examining the impact of irregular welding surface finishing versus the internal orientation defects of the samples. It is noteworthy that the height of the weld height was consistently maintained at no more than 10% of the overall weld width, adhering to the guidelines outlined in EN 1993-1-9. The test setup was configured based on the yield stress of the two materials in question. As high cycle fatigue typically involves minimal material plasticization, the maximum test stress was designated at a value lower than the yield stress of both materials. In order to construct the S–N curve, three stress range ($\Delta\sigma$) steps were selected. For each of these steps, three samples were subjected to testing. The selected $\Delta\sigma$ values were 252 MPa, 216 MPa, and 180 MPa, with a stress ratio (R) of 0.1. Post-testing, the fracture surfaces were scrutinized under a Scanning Electron Microscope (SEM) to ascertain the crack origin. The objective was to understand its correlation with the fatigue life and the build directions of the joint. The experimental procedure was implemented on two sets of samples wherein LPBF plates were welded to hot-rolled steel depending on their build direction to uncover and quantify any potential correlations between this orientation and its high cycle fatigue life.

The fatigue performance of two sets of welded samples was examined under cyclic uniaxial loads using the experimental configuration described in Table 3, where h represents the height of the sample, w denotes the thickness, A indicates the cross-sectional area, and h_w represents the height of the welding. The high cycle fatigue test results, including stress range ($\Delta\sigma$) and number of cycles to failure (N_f), were recorded in Table 4. Stress ranges are derived in terms of isotropic nominal stress by dividing the applied load for the nominal area. No failure was observed at the interface between the conventional steel part and the weld seam, or in the base conventional steel. To further investigate this phenomenon, the microstructure of the weld seam and its neighborhood were examined, as shown in Fig. 11.

The results indicated that the welded material exhibited better coupling with the conventional steel than with the LPBF part. The LPBF-weld seam interface showed a clean line, while the conventional steel exhibited a deeper penetration. Comparing the interface of the two LPBF parts, the Vertical samples showed better join with the weld seam than the Horizontal ones. This difference was taken into account during the analysis of the fatigue test results, and is discussed in detail in the following paragraphs. Regarding the results, it was found that most of the Vertical samples failed in the LPBF part, with only one sample experiencing run out, and another breaking at the weld toe, as shown in Fig. 12-a.

5. Fatigue behavior of the welded LPBF-quarto plate samples

An analysis on the detail category of the LPBF welded samples has been carried out to evaluate the slope of the mean values curve (m) from their experimental data, and to compare the resulting detail category with the standard ones from EN 1993-1-9 [14]. The results are classified according to the applied stress range, the LPBF build orientation and the failure crack location or possible run out. The statistical analysis has been performed with a 95% confidence level following ASTM E739 standard procedure [31], and it has been applied to both sets of samples (Vertical and Horizontal) considering them, first, as a unique set, and then one by one. The first statistical analysis has been performed by considering the Vertical and Horizontal samples as a homogeneous set. This identified a slope m=4.1 for the mean values curve (Fig. 13-a) and a stress range $\Delta\sigma_c$ = 115 MPa at 2 million cycles. The defined detail category is higher than the typical detail category for transverse butt-welds in plates. Indeed, by plotting the detail category curve with the conventional steel slope m=3 with a 95% confidence level (Fig. 13-b), the weakest Horizontal samples did not fit the obtained band. Investigating now the Vertical and Horizontal as independent sets, the statistical analysis highlighted two different trends (Fig. 13-c-d). The mean values from the Vertical set resulted in a curve having slope m=2.8, which is much steeper than the Horizontal one, which showed a slope m=7.4. This strong difference is due to the variability in the strength of the bond between the Horizontal base LPBF metal, and the weld seam. It is related to the microstructural

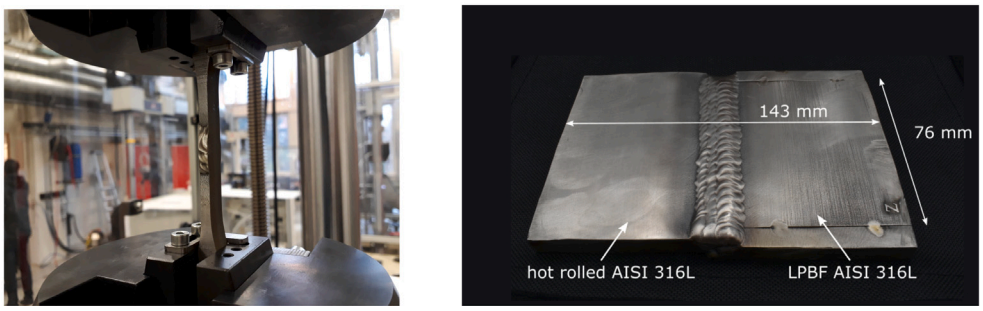

Fig. 10. Testing layout: (a) fatigue samples, (b) production plate.

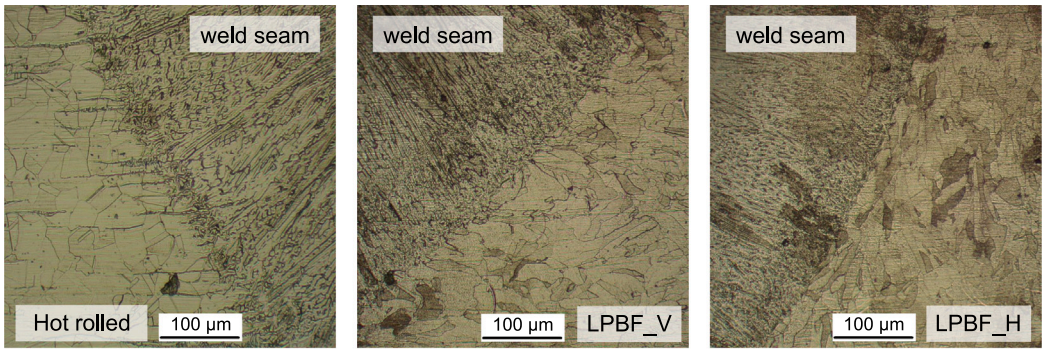

Fig. 11. Microstructure at the interface between the weld seam and the conventional steel, Vertical and Horizontal LPBF plate.

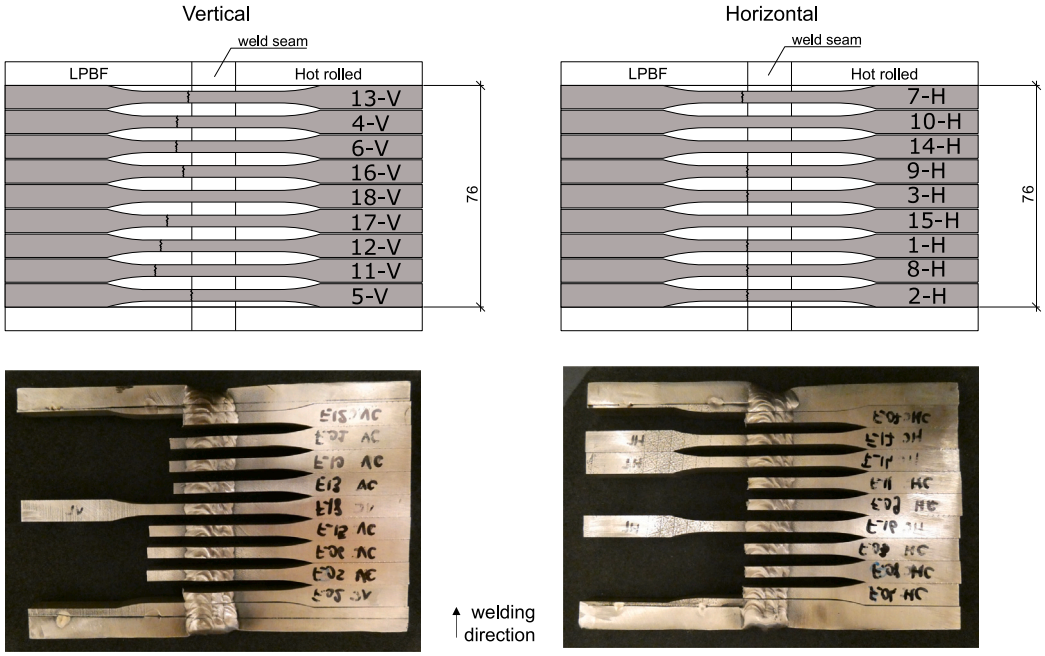

Fig. 12. Tested samples highlighting the fracture location.

properties and to the uncertainties of manual welding. Indeed, manual arc welding is affected by the possible instabilities of the starting and ending phases of the process, and it is a relevant cause of imperfections and defect generation. On the other hand, the vertically oriented samples showed a behavior close to the conventional steel butt welds, resulting in a mean values curve having slope m=2.8, and a stress range at 2 million cycles equal to 101 MPa, close to the detail category for transverse but welds.

The results have also been compared to the S–N curve from EN1993-1-9 prescribed for the detail category 90, according to the transverse

Table 3
Fatigue tests geometrical characteristics.

Id.	Orientation	Length [mm]	h [mm]	w [mm]	A [mm^2]	h_{ai} [mm]
1-H	Horizontal	138.9	10.2	4.0	40.8	11.0
2-H	Horizontal	140.0	10.1	4.1	41.4	10.5
3-H	Horizontal	139.8	9.8	4.2	41.2	11.2
4-V	Vertical	140.0	10.0	4.1	41.0	10.0
5-V	Vertical	140.4	10.2	4.0	40.8	11.0
6-V	Vertical	140.0	10.1	4.0	40.4	11.0
7-H	Horizontal	140.5	9.9	4.1	40.6	11.0
8-H	Horizontal	140.2	10.0	4.0	40.0	11.5
9-H	Horizontal	140.3	10.0	4.1	41.0	11.2
10-H	Horizontal	140.2	9.7	4.2	40.7	11.0
11-V	Vertical	140.0	10.2	4.1	41.8	11.4
12-V	Vertical	140.3	10.0	4.0	40.0	10.7
13-V	Vertical	140.1	10.0	4.0	40.0	11.0
14-H	Horizontal	140.0	10.0	4.0	40.0	10.7
15-H	Horizontal	140.3	10.0	4.0	40.0	11.0
16-V	Vertical	140.8	10.1	4.0	40.4	10.6
17-V	Vertical	139.8	10.1	4.1	41.4	11.0
18-V	Vertical	140.0	10.0	4.1	41.0	10.7

Table 4
Experimental results of the fatigue tests.

Id.	σ_{max} [MPa]	σ_{min} [MPa]	σ_a [MPa]	$\Delta\sigma$ [MPa]	N_f	Crack location
1-H	280	28	126	252	218,189	weld toe LPBF
2-H	280	28	126	252	106,404	weld toe LPBF
3-H	280	28	126	252	496,523	weld toe LPBF
4-V	280	28	126	252	900,000	LPBF HAZ
5-V	280	28	126	252	289,079	weld toe LPBF
6-V	280	28	126	252	739,005	LPBF HAZ
7-H	240	24	108	216	1,653,666	LPBF HAZ
8-H	240	24	108	216	198,465	weld toe LPBF
9-H	240	24	108	216	1,072,559	weld toe LPBF
10-H	240	24	108	216	2,473,705	run out
11-V	240	24	108	216	623,965	LPBF HAZ
12-V	240	24	108	216	409,634	LPBF HAZ
13-V	240	24	108	216	468,374	LPBF HAZ
14-H	200	20	90	180	8,600,000	run out
15-H	200	20	90	180	8,000,000	run out
16-V	200	20	90	180	1,058,167	LPBF HAZ
17-V	200	20	90	180	2,272,294	LPBF HAZ
18-V	200	20	90	180	7,500,000	run out

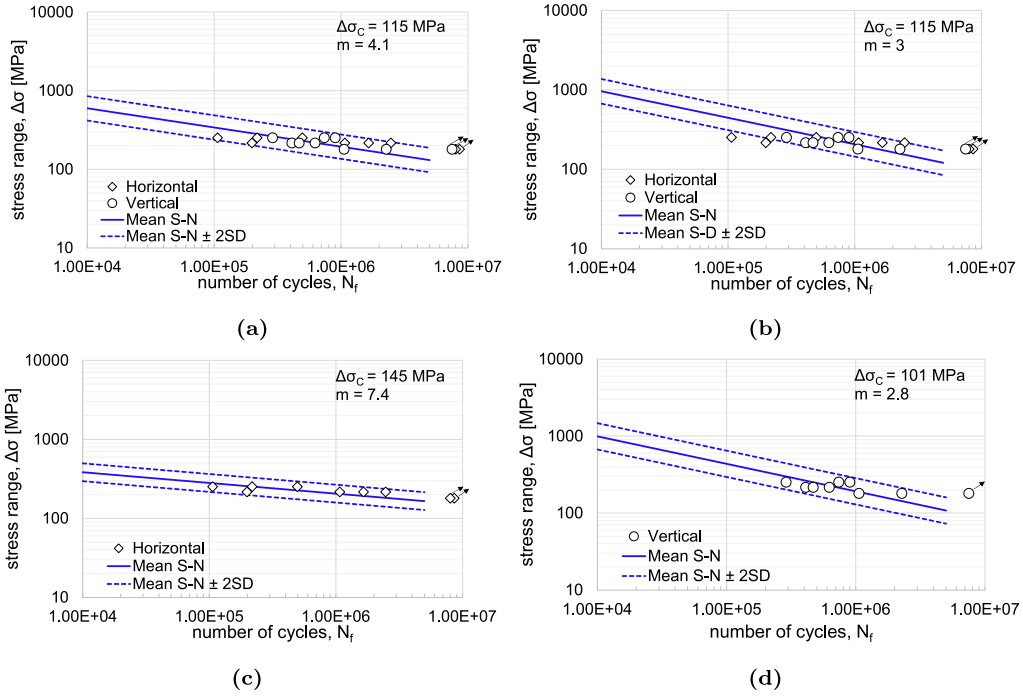

Fig. 13. S–N plot for the fatigue tests: (a) horizontal and vertical set (H+V); (b) horizontal and vertical set (H+V); (c) horizontal set (H); vertical set (V).

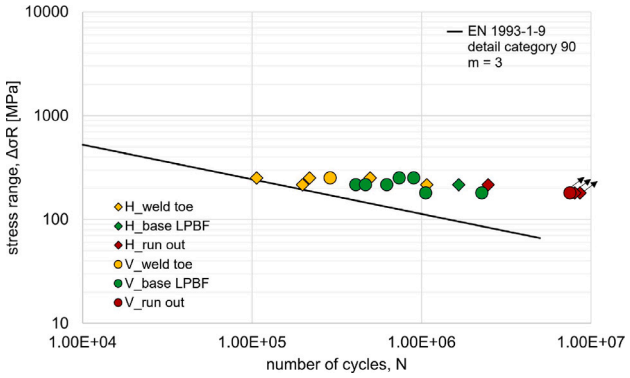

Fig. 14. S–N graph for the fatigue tests on the welded samples compared with the fatigue strength curve for direct stress ranges for detail category 90 from Eurocode 3 Part 1-9.

butt welds classification (Fig. 14). The aim of this comparison is to highlight if the hybrid welded samples respect the performance requirements prescribed by the international design standard despite the microscopic and behavior peculiarities due to LPBF manufacturing. The graph highlighted that all the results are above the design curve for a 75% confidence level of 95% probability of survival, thus all the tested samples verified the design limit from EN1993-1-9.

Stress range in Fig. 14 are derived in terms of isotropic nominal stress by dividing the applied load for the nominal area. By incorporating the anisotropy parameters in the numerical model, it is possible to characterize the stress variations in the vertical samples based on their build direction, as depicted in Fig. 9. Specifically, in this scenario, the stress levels for the vertical specimens are observed to decrease compared to the horizontal condition at equivalent strain levels. The results in terms of S–N plot are shown in Fig. 15 for only the vertical samples ($\Delta\sigma_c$ = 91, m=2.6) and for all the specimens ($\Delta\sigma_c$ = 106, m=3.8), showing a slightly lower fatigue detail category, still compatible with detail category 90 from Eurocode 3 Part 1-9.

Considering the reduced level of anisotropy, the application of the strain energy density (SED) approach becomes viable for fatigue analysis. The SED approach, as described in previous works by Berto et al. [41–43], involves evaluating the local strain energy density W within a predefined control volume surrounding the notch. This approach proves effective in providing accurate results for complex structures, even with a coarse mesh resolution, as it primarily relies on geometric parameters. A critical value W_C is defined within the SED method to determine fracture conditions. As for the control volume, it is determined by the radius R_0, which can be calculated using Eq. (8) specifically for V-notched specimens.

$$R_0 = \left[\frac{I_1}{4\lambda_1(\pi-\alpha)}\left(\frac{K_{1C}}{\sigma_t}\right)^2\right]^{1/2(1-\lambda_1)} \tag{8}$$

In this equation, I_1 is influenced by the opening angle of the notch and Poisson's ratio, resulting in different values under plane stress and plane strain conditions. λ_1 represents Williams' mode I eigenvalue, K_{1C} is the material toughness, α is the corner angle and σ_t is the conventional ultimate tensile strength. For mode I loading scenarios, the average value of the elastic strain energy density (SED) can be defined as given in Eq. (9).

$$\Delta W = \frac{I_1}{4\lambda_1(\pi-\alpha)}\left(\frac{K_1}{R_0^{1-\lambda_1}}\right)^2 \tag{9}$$

where K_1 corresponds to the notch stress intensity factor. The expression for K_1, specifically for sharp V notches, is presented in Eq. (11).

$$K_1 = \sqrt{2\pi}\,lim\; r^{1-\lambda_1}\left[\sigma_{\vartheta\vartheta}(r,0)\right] \tag{10}$$

Table 5
SED analysis results.

Id.	$\Delta W(R_0 = 0.28)$	N_f	Crack location
1-H	0.706	218,189	weld toe LPBF
2-H	0.706	106,404	weld toe LPBF
3-H	0.706	496,523	weld toe LPBF
4-V	0.191	900,000	LPBF HAZ
5-V	0.722	289,079	weld toe LPBF
6-V	0.191	739,005	LPBF HAZ
7-H	0.136	1,653,666	LPBF HAZ
8-H	0.513	198,465	weld toe LPBF
9-H	0.513	1,072,559	weld toe LPBF
10-H	–	2,473,705	run out
11-V	0.139	623,965	LPBF HAZ
12-V	0.140	409,634	LPBF HAZ
13-V	0.139	468,374	LPBF HAZ
14-H	0.350	8,600,000	run out
15-H	0.350	8,000,000	run out
16-V	0.098	1,058,167	LPBF HAZ
17-V	0.098	2,272,294	LPBF HAZ
18-V	–	7,500,000	run out

in which $\sigma_{\vartheta\vartheta}$ represents the tangential stress considering the polar coordinates system (r, ϑ). In accordance with established engineering approximations for structural steels [42], the critical radius R_0 has been adopted as 0.28 mm in this study. According to Berto et al. [44], the formulation of Strain Energy Density can be revised by incorporating the linear elastic normal and shear stress components in the polar frame of reference, represented as $\sigma_{\theta\theta,\theta=0,peak}$ and $\tau_{r\theta,\theta=0,peak}$. Consequently, an equivalent peak stress under plain strain conditions, denoted as $\sigma_{eq,peak}$, can be derived and extracted from Finite Element (FE) models. The governing relationship for the SED is elucidated as follows:

$$\Delta W = \frac{1-\nu^2}{E}\Delta\sigma_{eq,peak}^2 \tag{11}$$

Fig. 16-a displays the outcomes from the conducted experimental campaign, and the corresponding results are listed in Table 5. Additionally, Fig. 16-b showcases the superimposition of the experimental results for steel butt-welded joints with the design scatter band (adapted from Berto and Lazzarin [45]). The results depicted in Fig. 16 show a distinct discrepancy in the average strain density between the weld toe samples and LPBF specimens. Furthermore, a significant variation is evident in the SED values between the vertical and horizontal samples, with the horizontal direction displaying higher SED values in comparison to the vertical orientation. Consequently, the cause of these observations prompts further investigation into the location of crack formation or the formation of critical internal defects, contingent upon the sample's specific location.

6. Fracture surface

To deeper investigate the fatigue behavior of the welded samples, the fracture surface of each tested sample has been analyzed to possibly relate the number of cycles to failure with: the presence of defects; the location and dimension of these defects; the build orientation of the LPBF part. The samples with the lowest N_f showed an advancing crack front located at the interface between the LPBF and the weld seam (Fig. 17-a). With higher fatigue life, the samples showed diffused internal defects for the Vertical samples (Fig. 17-b), and surface defects for the horizontally oriented (Fig. 17-c).

Then, the number of internal defects decreased, and at the highest N_f, the crack formation was induced by just a single defect (Fig. 17-d). By neglecting the failure due to welding-induced defects, a dependency on the build orientation can be observed. The vertically oriented samples showed crack formation in the base metal due to more critical internal defects. However, the porosity analysis performed in the previous section did not reveal significant differences between the two orientations. However, by considering that the defects develop with an

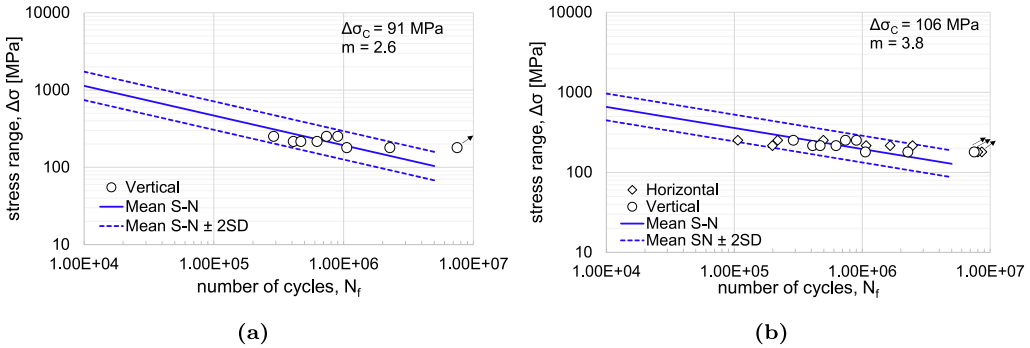

Fig. 15. S–N plot considering material anisotropy: (a) vertical set (H+V); (b) horizontal and vertical set (H+V).

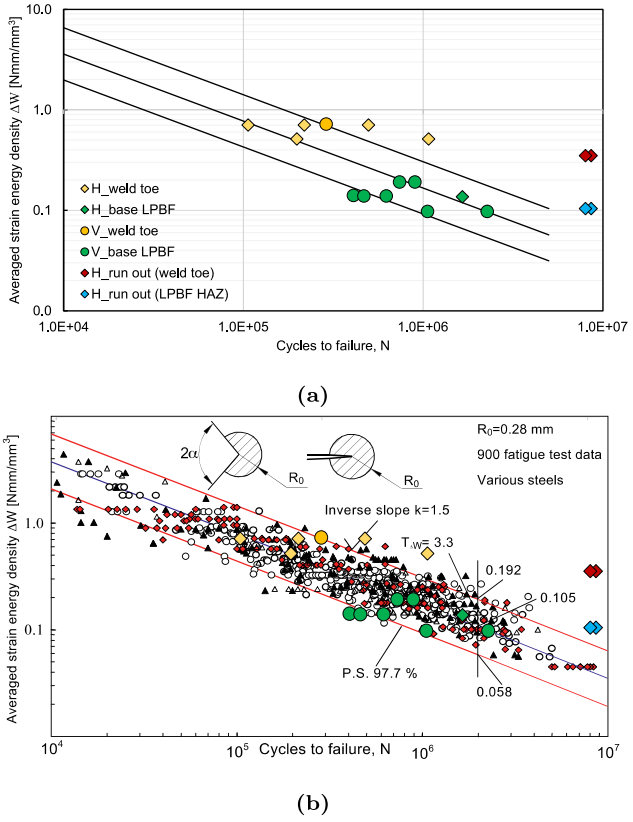

Fig. 16. Average strain density vs number of cycles for the fatigue tests for the current experimental campaign (a); comparison with steel butt-welded joints [45] (b).

elongated shape directed orthogonally to the build direction of the component, the Horizontal samples had their defects oriented according to the applied load, while the Vertical ones were orthogonal to the test direction. This means that higher stress and strain concentrations are generated on the Vertical samples' defects, causing a higher sensitivity to cyclic loads.

7. Discussion

The fatigue behavior is a hot topic for LPBF products, especially because their typical porosity and anisotropy reduce the predictability of the fatigue life. The aim of the tests and analyses was to identify the weakest part of welded samples, relate the fatigue life with the build direction of the LPBF part, and compare their S–N curve with the EN1993-1-9 detail categories. The analysis demonstrated that the hybrid welded butt joint respected the performance provision set by EN1993-1-9 for butt joints (Detail category 90). It means that for high cycle fatigue, LPBF products may have a comparable behavior to homogeneous steel but-joint, and it opens new possibilities to AM in the realm of construction.

Upon delving deeper into the experimental results, a correlation emerged between the gradient of the S–N curve and the build orientation of the LPBF elements, facilitating the discovery of distinct detail categories. This indicates that the anisotropy of LPBF metals impacts fatigue life, considering not only the dimensions and orientation of internal defects but also their compatibility with the welded elements.

When comparing vertically oriented LPBF samples with their horizontally oriented counterparts in the welded LPBF to conventional AISI 316L, the former exhibited inferior fatigue behavior. This can be attributed to the presence of transversely oriented internal defects relative to the load direction. Furthermore, the strain energy density-based analysis of the vertical and horizontal samples highlighted higher SED values and discrepancies favoring the horizontal direction over the vertical one. Although this finding carries significance, it should be noted that research into the fatigue life of LPBF products intended for structural applications remains in its nascent stages.

Similar findings were reported in previous studies [46,47]. Specifically, Beretta et al. [46] examined the influence of surface roughness on the fatigue behavior of L-PBF AlSi10Mg printed in five different build directions. The results of their fatigue testing demonstrated that the horizontal specimens exhibited higher fatigue limits compared to the vertical series.

However, the classification of the weakest points within LPBF hybrid products showed that the fatigue behavior is mainly a function of roughness as shown in previous studies [48–51] causing stress concentration effects [30,52]. In particular, Elangeswaran et al. [30] carried out a fatigue test campaign on miniaturized LPBF samples, showing that the non-machined surface exhibits a micronotch effect, leading to early crack initiation. Machining removes these stress concentration sites, resulting in enhanced fatigue performance. In the current study, among the horizontal oriented samples, the most critical defect was identified as the bonding between the weld seam and the LPBF steel. These joints showed a lower sensitivity to internal defects in the LPBF steel, as evidenced by the occurrence of run-out (10-H, 14-H, 15-H) when a strong bond was formed between the weld seam and the LPBF element. In contrast, when the samples incorporated a vertically oriented LPBF part, the bond between the weld seam and the LPBF part proved to be more robust compared to the material internal defects and the cracks tend to locate in the LPBF HAZ.

8. Conclusions

In conclusion, this research aimed to investigate the fatigue life of hybrid welded butt joints, which involved a hot-rolled plate welded to an LPBF counterpart, both fabricated using AISI 316L. The primary objective was to compare the application of conventional materials in

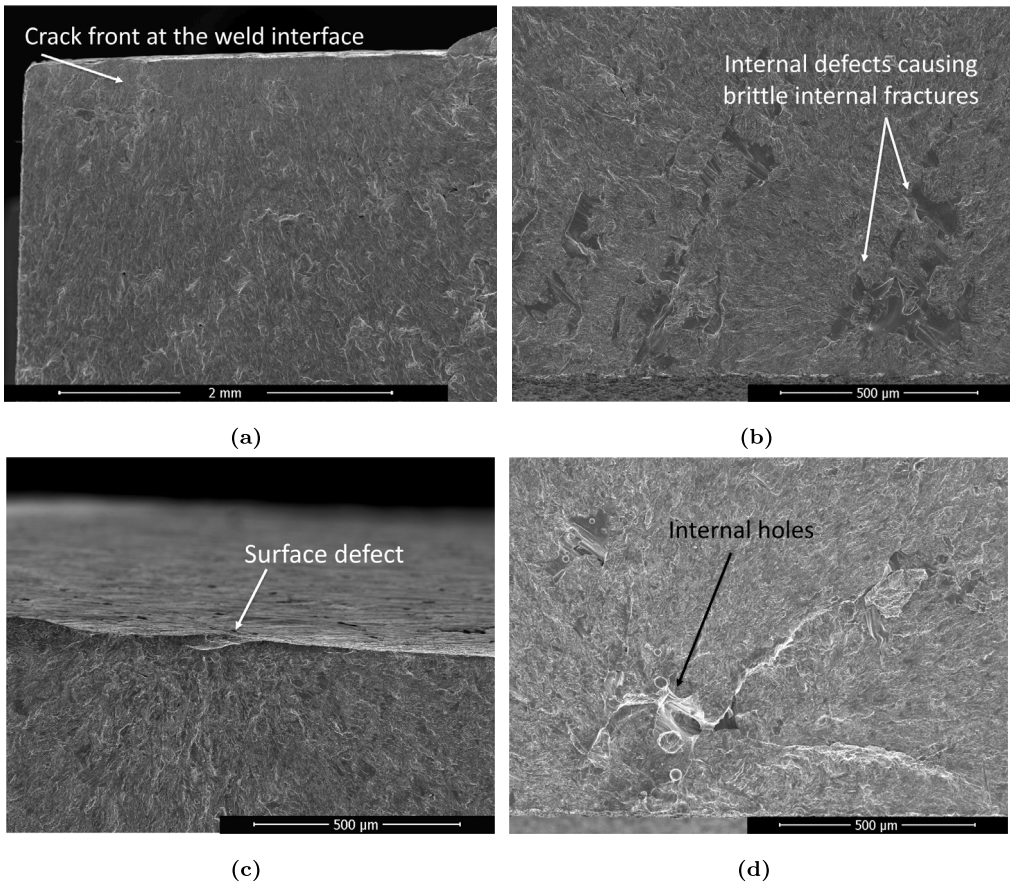

Fig. 17. Fracture surfaces of the fatigue tests samples: (a) crack front located at the interface; (b) internal defects for the Vertical samples; (c) surface defects for the Horizontal samples; (d) crack formation from single defect.

construction details with the potential application of metal Additive Manufacturing (AM) through hybrid manufacturing techniques.

The study comprised two main parts. Firstly, the anisotropic behavior of hybrid specimens during the elastic phase was analyzed and modeled. Calibration of the models was performed based on experimental static tests, considering the strain/stress relationship with respect to the samples' build direction. In the second part, the high cycle fatigue of hybrid LPBF-quarto plate samples was investigated using the S–N curves approach following ASTM E739-19 guidelines. The orientation, geometry, and dimensions of defects were identified as the primary factors influencing failure.

The findings of this study contribute valuable insights to enhance the understanding of the fatigue life of LPBF products and identify critical features that impact the fatigue life of joints. Notably, the study revealed that the weld seam-LPBF steel interface was the most critical defect when horizontally oriented LPBF parts were employed. Moreover, vertically built samples exhibited a shorter fatigue life compared to their horizontally built counterparts.

These findings have significant implications for calculating the fatigue life of structures. For samples perpendicular to the build direction, the fatigue detail category may decrease by up to 30% when using a nominal stress definition ($\Delta\sigma_c$ = 101 MPa vs $\Delta\sigma_c$ = 145 MPa) and up to 37% when considering anisotropic behavior ($\Delta\sigma_c$ = 91 MPa). Therefore, it is crucial to consider these factors and develop guidelines to facilitate the potential application of LPBF products in the construction sector.

Furthermore, the results demonstrated that the hybrid welded butt joint met the performance requirements set by EN 1993-1-9 for butt joints, specifically achieving a fatigue detail category of 90. This indicates that LPBF products exhibit comparable behavior to homogeneous steel butt joints in terms of high cycle fatigue. Consequently, there is considerable potential to effectively integrate these technologies into actual structures, either for the realization of new joints or the localized repair of damaged ones.

CRediT authorship contribution statement

Alessandro Menghini: Conceptualization, Methodology, Data curation, Writing – original draft, Project administration. **Martina Chierici:** Conceptualization, Methodology, Software, Data curation, Writing. **Alper Kanyilmaz:** Reviewing & editing, Supervision, Funding acquisition, Project administration. **Ali Gökhan Demir:** Supervision, Reviewing & editing, Funding acquisition, Project administration. **Carlo Andrea Castiglioni:** Supervision, Funding acquisition, Project administration. **Filippo Berto:** Supervision, Funding acquisition, Project administration. **Barbara Previtali:** Supervision, Funding acquisition, Project administration.

Declaration of competing interest

The authors declare that they have no known competing financial interests or personal relationships that could have appeared to influence the work reported in this paper.

Data availability

Data will be made available on request.

Acknowledgment

The authors acknowledge CIMOLAI S.p.A. for the technical support and expertise in the field, and for providing the case study details.

Open access funding is provided by Politecnico di Milano within the CRUI-CARE Agreement. This work has been realised as a preliminary study for the research project CONSTRUCTADD EURFCS 101057957 (http://www.constructadd.eu) [53], funded by the European Union. Views and opinions expressed are, however, those of the authors only and do not necessarily reflect those of the European Union or Research Fund for Coal and Steel. Neither the European Union nor the Research Fund for Coal and Steel can be held responsible for them.

References

[1] T. DebRoy, et al., Scientific, technological and economic issues in metal printing and their solutions, Nat. Mater. 18 (10) (2019) 1026–1032.
[2] Daniel Delgado Camacho, et al., Applications of additive manufacturing in the construction industry–A forward-looking review, Autom. Constr. 89 (2018) 110–119.
[3] Craig Buchanan, Leroy Gardner, Metal 3D printing in construction: A review of methods, research, applications, opportunities and challenges, Eng. Struct. 180 (2019) 332–348.
[4] Martina Chierici, Filippo Berto, Alper Kanyilmaz, Resource-efficient joint fabrication by welding metal 3D-printed parts to conventional steel: A structural integrity study, Fatigue Fract. Eng. Mater. Struct. 44 (5) (2021) 1271–1291.
[5] Aref Yadollahi, Nima Shamsaei, Additive manufacturing of fatigue resistant materials: Challenges and opportunities, Int. J. Fatigue 98 (2017) 14–31.
[6] Pietro Foti, et al., Multiaxial fatigue of additively manufactured metallic components: A review of the failure mechanisms and fatigue life prediction methodologies, Prog. Mater. Sci. 137 (2023) 101126.
[7] Leroy Gardner, Metal additive manufacturing in structural engineering–review, advances, opportunities and outlook, in: Structures, vol. 47, Elsevier, 2023.
[8] Cheng Huang, et al., Fatigue testing and analysis of steel plates manufactured by wire-arc directed energy deposition, Addit. Manuf. (2023) 103696.
[9] Cheng Huang, et al., Fatigue crack growth behaviour of wire arc additively manufactured steels, Int. J. Fatigue 173 (2023) 107705.
[10] Ragul Gandhi, Lorenzo Maccioni, Franco Concli, Significant advancements in numerical simulation of fatigue behavior in metal additive manufacturing-review, Appl. Sci. 12 (21) (2022) 11132.
[11] Alper Kanyilmaz, et al., Role of metal 3D printing to increase quality and resource-efficiency in the construction sector, Addit. Manuf. 50 (2022) 102541.
[12] D. Radaj, C.M. Sonsino, W. Fricke, Recent developments in local concepts of fatigue assessment of welded joints, Int. J. Fatigue 31 (1) (2009) 2–11.
[13] Finn Sallaba, et al., Relation between the fatigue and fracture ductile–brittle transition in S500 welded steel joints, Metals 12 (3) (2022) 385.
[14] CEN. Eurocode 1993-1-9: Design of Steel Structures, Part 1.9: Fatigue, European Committee for Standardisation;, 2003.
[15] A. Riemer, et al., On the fatigue crack growth behavior in 316L stainless steel manufactured by selective laser melting, Eng. Fract. Mech. 120 (2014) 15–25.
[16] M. Zhang, et al., Fatigue and fracture behaviour of laser powder bed fusion stainless steel 316L: Influence of processing parameters, Mater. Sci. Eng. A 703 (2017) 251–261.
[17] F. Zeng, Y. Yang, G. Qian, Fatigue properties and S-N curve estimating of 316L stainless steel prepared by SLM, Int. J. Fatigue 162 (January) (2022) 106946.
[18] Joe Elambasseril, et al., Laser powder bed fusion additive manufacturing (LPBF-AM): the influence of design features and LPBF variables on surface topography and effect on fatigue properties, Crit. Rev. Solid State Mater. Sci. 48 (1) (2023) 132–168.
[19] Jason Rogers, et al., Fatigue test data applicability for additive manufacture: A method for quantifying the uncertainty of AM fatigue data, Mater. Des. (2023) 111978.
[20] Ruizhi Zhang, et al., Mechanical properties and microstructure of additively manufactured stainless steel with laser welded joints, Mater. Des. 208 (2021) 109921.
[21] Petr Mohyla, et al., Analysis of welded joint properties on an AISI316L stainless steel tube manufactured by SLM technology, Materials 13 (19) (2020) 4362.
[22] Marion Merklein, Robert Schulte, Thomas Papke, An innovative process combination of additive manufacturing and sheet bulk metal forming for manufacturing a functional hybrid part, J. Mater Process. Technol. 291 (2021) 117032.
[23] T. Pasang, et al., Microstructure and mechanical properties of welded additively manufactured stainless steels SS316L, Met. Mater. Int. 25 (2019) 1278–1286.
[24] Martina Chierici, et al., Hybrid manufacturing of steel construction parts via arc welding of LPBF-produced and hot-rolled stainless steels, Prog. Addit. Manuf. (2023) 1–22.
[25] B. Previtali, et al., Comparative costs of additive manufacturing vs. machining: the case study of the production of forming dies for tube bending, in: 2017 International Solid Freeform Fabrication Symposium, University of Texas at Austin, 2017.
[26] Ugur M. Dilberoglu, et al., Current trends and research opportunities in hybrid additive manufacturing, Int. J. Adv. Manuf. Technol. 113 (2021) 623–648.
[27] Messele Sefene Eyob, Yeabsra Mekdim Hailu, Assefa Asmare Tsegaw, Metal hybrid additive manufacturing: state-of-the-art, Prog. Addit. Manuf. 7 (4) (2022) 737–749.
[28] Lan Kang, et al., Residual stresses in circular steel tubular columns repaired by laser-cladding additive manufacturing, Thin-Walled Struct. 193 (2023) 111275.
[29] Alessandro Menghini, An approach for fatigue assessment of existing steel bridges, 2023.
[30] A. Menghini, A. Kanyilmaz, F. Berto, Fatigue stress concentration factor reduction via metal additive manufacturing, Strength Mater. (2023) 1–7.
[31] ASTM E739-10(2015) Standard Practice for Statistical Analysis of Linear or Linearized Stress-Life (S-N) and Strain-Life (ϵ-N) Fatigue Data.
[32] European Committee for Standardization, EN 1090-1 (2009) execution of steel structures and aluminium structures—part 1: requirements for conformity assessment of structural components, 2011.
[33] ASTM International, ASTM F3184-16. Standard specifcation for additive manufacturing stainless steel alloy (UNS S31603) with powder bed fusion, 2016, pp. 1–9, ICS Code: 25 (030).
[34] European Committee for Standardization, E.N. 1993-1-4 (2006): Eurocode 3: Design of steel structures - Part 1-4: General rules - supplementary rules for stainless steel, 2006, pp. 1–35.
[35] European Committee for Standardization, EN 1993-1-5 (2006) eurocode 3 - Design of steel structures - Part 1-5: Plated structural elements, 2006.
[36] H. Ding, W. Chen, L. Zhang, Elasticity of transversely isotropic materials, Vol. 126, Springer Science & Business Media, 2006.
[37] E.V. Morozov, V.V. Vasiliev, Determination of the shear modulus of orthotropic materials from off-axis tension tests, Compos. Struct. 62 (3–4) (2003) 379–382.
[38] M. Smith, ABAQUS/Standard User's Manual, Version 6.9, Dassault Systèmes Simulia Corp, 2009.
[39] Yihong Kok, et al., Anisotropy and heterogeneity of microstructure and mechanical properties in metal additive manufacturing: A critical review, Mater. Des. 139 (2018) 565–586.
[40] Alexander E. Wilson-Heid, et al., Quantitative relationship between anisotropic strain to failure and grain morphology in additively manufactured Ti-6Al-4V, Mater. Sci. Eng. A 706 (2017) 287–294.
[41] F. Berto, P. Lazzarin, Recent developments in brittle and quasi-brittle failure assessment of engineering materials by means of local approaches, Mater. Sci. Eng. R 75 (2014) 1–48.
[42] Pietro Foti, Filippo Berto, Fatigue assessment of high strength welded joints through the strain energy density method, Fatigue Fract. Eng. Mater. Struct. 43 (11) (2020) 2694–2702.
[43] Claas Fischer, Wolfgang Fricke, Cesare M. Rizzo, Experiences and recommendations for numerical analyses of notch stress intensity factor and averaged strain energy density, Eng. Fract. Mech. 165 (2016) 98–113.
[44] Giovanni Meneghetti, Alberto Campagnolo, Filippo Berto, Fatigue strength assessment of partial and full-penetration steel and aluminium butt-welded joints according to the peak stress method, Fatigue Fract. Eng. Mater. Struct. 38 (12) (2015) 1419–1431.
[45] Paolo Lazzarin, Filippo Berto, Michele Zappalorto, Rapid calculations of notch stress intensity factors based on averaged strain energy density from coarse meshes: Theoretical bases and applications, Int. J. Fatigue 32 (10) (2010) 1559–1567.
[46] S. Beretta, et al., Fatigue strength assessment of as built AlSi10Mg manufactured by SLM with different build orientations, Int. J. Fatigue 139 (2020) 105737.
[47] A. Du Plessis, S. Beretta, Killer notches: The effect of as-built surface roughness on fatigue failure in AlSi10Mg produced by laser powder bed fusion, Addit. Manuf. 35 (2020) 101424.
[48] Chola Elangeswaran, et al., Predicting fatigue life of metal LPBF components by combining a large fatigue database for different sample conditions with novel simulation strategies, Addit. Manuf. 50 (2022) 102570.
[49] Antonio Cutolo, et al., Fatigue life prediction of a L-PBF component in Ti-6Al-4V using sample data, FE-based simulations and machine learning, Int. J. Fatigue 167 (2023) 107276.
[50] Joy Gockel, et al., The influence of additive manufacturing processing parameters on surface roughness and fatigue life, Int. J. Fatigue 124 (2019) 380–388.
[51] Jonathan Pegues, et al., Surface roughness effects on the fatigue strength of additively manufactured Ti-6Al-4V, Int. J. Fatigue 116 (2018) 543–552.
[52] Chola Elangeswaran, et al., Predicting fatigue life of metal LPBF components by combining a large fatigue database for different sample conditions with novel simulation strategies, Addit. Manuf. 50 (2022) 102570.
[53] Alper Kanyilmaz, 2023, https://alperkanyilmaz.com/.